IEEE Access
Multidisciplinary ⋮ Rapid Review ⋮ Open Access Journal

Received 13 June 2023, accepted 23 June 2023, date of publication 27 June 2023, date of current version 6 July 2023.

Digital Object Identifier 10.1109/ACCESS.2023.3289976

RESEARCH ARTICLE

The Estimation Method of Sensing Parameters Based on OTFS

ZHILING TANG, ZHOU JIANG, WANGHUA PAN, AND LIZHEN ZENG
Guangxi Key Laboratory of Wireless Broadband Communication and Signal Processing, School of Information and Communication, Guilin University of Electronic Technology, Guilin 541004, China

Corresponding author: Zhiling Tang (tzl888@guet.edu.cn)

This work was supported by the Guangxi Natural Science Foundation under Grant 2021GXNSFAA220010.

ABSTRACT In an integrated sensing and communication (ISAC) system, improving the accuracy of delay and Doppler shift sensing parameter estimation is a critical task that sustains the performance of the communication system. To tackle this task, we introduce a two-stage estimation algorithm named matched filter-Fibonacci (MF-F), which employs the orthogonal time frequency space (OTFS) waveform characteristics in the delay-Doppler (DD) domain. In the first step (MF), the sensing parameters are approximated on an integer grid using the relationship between the input and output signals of the DD domain ISAC model. This approximation is executed on an integer grid using the cyclic shift property of the matrix. In the following step (F), we implement a two-dimensional (2D) searching technique based on the Fibonacci sequence, called the Fibonacci search method, to achieve sensing parameter estimation with fractional accuracy. This method decreases the number of comparisons needed and enhances the search process speed. Finally, the proposed method in this study was tested using numerical simulations and hardware experiments. The results demonstrate that the MF-F method can precisely estimate the speed and distance with millimeter-level accuracy and has the robustness and low complexity in numerical simulation. Moreover, the hardware experiment's estimated Doppler and delay parameters can reach the centimeter and meter levels.

INDEX TERMS Integrated sensing and communication (ISAC), signal modulation, delay-Doppler (DD) domain super-resolution estimation, low complexity.

I. INTRODUCTION

Various research has been conducted on 6G technology, including the exploration of the vision and challenges of 6G technology [1], [2], [3]. The research focuses on the design of the integrated sensing and communication (ISAC) waveform [4], [5], [6]. Other research areas include wireless propagation path prediction and electromagnetic spectrum mapping [7], terahertz technology [8], and the construction of the metaverse [9]. The integration of radar sensing and wireless communication is a crucial research topic, as it can enhance spectrum utilization and reduce maintenance costs through shared equipment. However, this integration also presents several challenges, including hardware implementation, signal processing, information theory, and ISAC performance metrics [10], e.g., when ISAC devices operate in full-duplex mode, the simultaneous use of communication transmitters and radar sensing receivers in an environment of high device density, complex functionalities, and spectrum congestion may lead to significant self-interference and cross-interference, which hinders signal detection. Furthermore, due to the interdependence of these devices, there is an increased risk of mutual interference. Hence, intelligent interference cancellation technology development has become a crucial research field that requires further exploration. The design of waveforms that satisfy radar sensing and data communication requirements is challenging. While radar sensing systems have traditionally utilized waveforms optimized for detection performance, communication systems generally employ standardized waveforms optimized

The associate editor coordinating the review of this manuscript and approving it for publication was Walid Al-Hussaibi.

This work is licensed under a Creative Commons Attribution-NonCommercial-NoDerivatives 4.0 License.
For more information, see https://creativecommons.org/licenses/by-nc-nd/4.0/

for communication purposes [9]. Recently, orthogonal time frequency space (OTFS) modulation technology was first presented by [11]. Following the introduction, a further examination into OTFS pulse shaping [12], channel estimation [13], and signal detection are conducted in [14], [15]. Their studies, which focused on the technical aspects of this technology, were subsequently documented and summarized in [16]. In contrast, different techniques, such as multiple signal classification methods (MUSIC) [17] and noise subspace methods [18], require feature decomposition and numerous matrix-vector multiplications. Authors in [19] and [20] respectively proposed the fast Fourier transform (FFT) method and the fast cyclic cross-correlation (FCCC) detection method to estimate velocity and distance via the generation of range-Doppler maps (RDMs) followed by the use of a cell-averaging constant false-alarm rate detector (CA-CFAR). Although this RDM-based approach effectively detects singular targets, it performs poorly in multi-target scenarios and needs millimeter-level precision in parameter estimation. Moreover, generating a two-dimensional (2D) RDM matrix and detecting it using CA-CFAR translates to high complexity and computational requirements. A more adaptable and tractable approach, known as virtual cyclic prefix (VCP), was proposed by [21]. This approach operates in the Fourier domain, simplifying computational complexity. The OTFS radar sensing system utilizes the atomic norm by minimizing it [22]. This is achieved by solving the convex optimization problem using the alternating direction method of multipliers (ADMM). The 2D MUSIC algorithm is then employed to search for the solution obtained to propose an excellent high-resolution parameter estimation method.

The OTFS waveform offers several advantages when used in the ISAC system:

- OTFS is capable of overcoming time-selective fading caused by Doppler frequency shift. When the velocity of objects affecting the channel is constant, the time-varying channel appears constant in the delay-Doppler domain. Therefore, adaptive modulation and coding schemes are unnecessary [23]. This is particularly significant for rapidly changing channels since the timely acquisition of the latest channel state information at the transmitter is challenging.
- The OTFS system functions in the delay-Doppler (DD) domain where radar targets are situated, and the channel and sensing parameters are connected in the same domain. Due to this, the inherent sparsity of the DD domain can be utilized [24]. Authors in [25] have established that the sensing performance of the OTFS system is as precise as that of orthogonal frequency division multiplexing (OFDM) and frequency-modulated continuous wave (FMCW).
- Radar sensing typically achieves a higher parameter estimation match filter gain than the channel estimation algorithm implemented in communication systems [26]. This is due to the use of the same physical channels at both transmission nodes and the radar receiver's knowledge of the information transmitted in a monostatic sensing scenario.

OTFS modulation relies on exploring and utilizing symbol reuse and channel characteristics in the delay-Doppler domain, which contrasts with the symbol reuse in the traditional time-frequency OFDM modulation [27]. The inherent sparsity of the DD channel can be leveraged for sensing and detection purposes, but the approach faces complexity and accuracy challenges:

- The author of [28] proposed a matched filtering (MF) algorithm that uses the OTFS radar system to estimate the distance and velocity of various targets. A significant drawback of the algorithm is its high computational complexity and inability to estimate fractional delay and Doppler shift, contributing to low sensing accuracy. Additionally, the algorithm can only improve the estimation accuracy of the target distance when discrete DD domain dimensions are sufficiently large.
- The estimation of target parameters is performed using the maximum likelihood detection (MLD) algorithm [29]. This algorithm demands an exhaustive search throughout the complete distance-Doppler region to determine the estimates for each tested distance-Doppler grid. High-dimensional matrix operations are executed for each tested distance-Doppler grid to calculate the metrics [20]. The ADMM-AN algorithm proposed in [22] exhibits high perceptual performance. However, to obtain its solution, it is necessary to conduct a search using the 2D MUSIC algorithm. Consequently, the computation complexity is high.
- The author of [30] introduced the algorithm for sensing parameter estimation with low computational complexity. The algorithm estimates distances with millimeter-level accuracy and velocities with decimeter-per-second level accuracy. However, the algorithm's velocity estimation could be more precise, reaching the decimeter level.

The existing sensing algorithms based on OTFS suffer from high complexity, low sensing parameter accuracy, and poor multi-target detection performance. To overcome these challenges, the matched filter-Fibonacci (MF-F) algorithm is proposed in this paper. MF-F is a two-stage solution that addresses both high complexity and low sensing parameter accuracy. The main contributions of this paper can be summarized as follows:

1) In the MF step, the input-output relationship is obtained through continuous DD channels. Subsequently, the ML algorithm searches for the sensing parameters of complex channel gain coefficients, time delay, and Doppler frequency shift in the DD channels. We estimate the complex channel gain coefficient by assigning values to time delay and Doppler frequency shift in order to reduce the search dimension of the ML algorithm. Then, we apply the ML algorithm to determine the parameters of sense. As a result, the estimated parameter

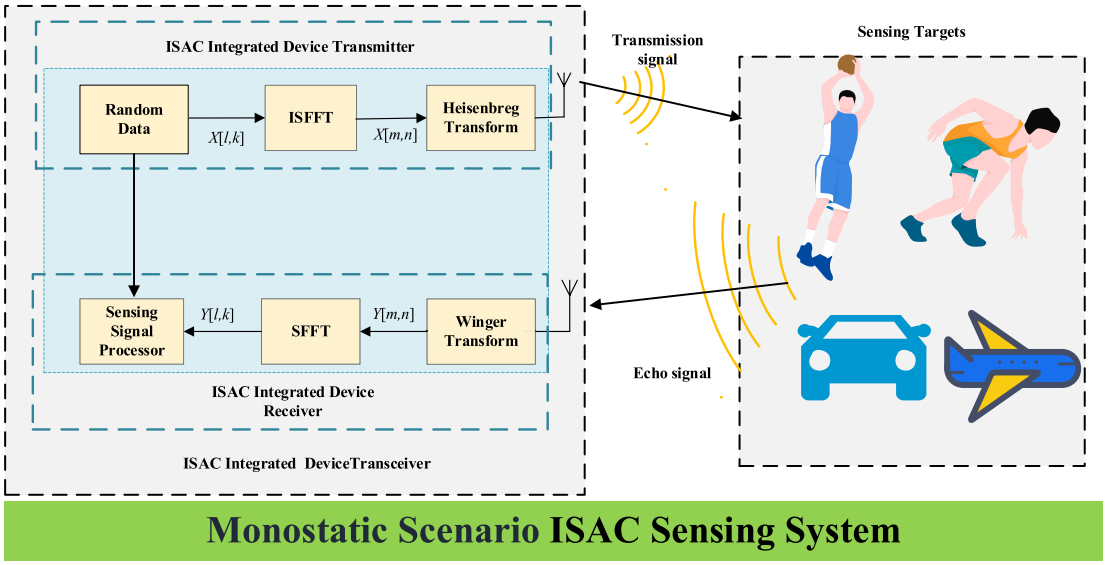

FIGURE 1. OTFS transmitter based on the IDZT using rectangular pulse shaping waveform ($M = 6, N = 6$).

search range is now reduced from three-dimensional (3D) to 2D.

2) In a scenario where monostatic sensing is used for communication, the transmission of information is known, and thus, it is possible to estimate complex channel gain coefficients through the input-output relationship matrix in the DD domain of the OTFS system. Since the transmission and reception information matrices are known, there is no need for high complexity. Subsequently, in the MF step, the estimated value of the integer grid is determined by e ML, allowing for the narrowing down of the super-resolution estimate range for the F step.
3) We propose a 2D Fibonacci search method in the F step to achieve a super-resolution estimation effect for a more precise estimation of score delay and Doppler frequency shift parameters.

The rest of this paper is structured as follows. Section II outlines the ISAC system model based on OTFS and provides a basis for the proposed OTFS-based sensing algorithm described in Section III. We present the numerical simulation results in Section IV, followed by the discussion and conclusions in Section V.

II. SENSING SYSTEM MODEL

Fig. 1 illustrates the monostatic sensing system which comprises a transmitter, receiver, and channel. The transmitter generates OTFS waveforms used for communication and sensing functions. Integrating a sensing receiver converts a communication-only node into an ISAC node. As the communication signal is transmitted, the sensing receiver gathers target echoes for perception. The self-interference is disregarded, where the signal leaks directly from the transmitter to the receiver due to the inherent full-duplex operation, similar to the perception systems discussed in [21] and [25]. Reflection of the target results in a backward scattering signal, which enables active perception. The radar sensing receiver, located at the transmitter end, captures and utilizes all transmitted signal information to estimate the parameters of the target. The paper utilizes matrices and vectors to represent the model of the perception system.

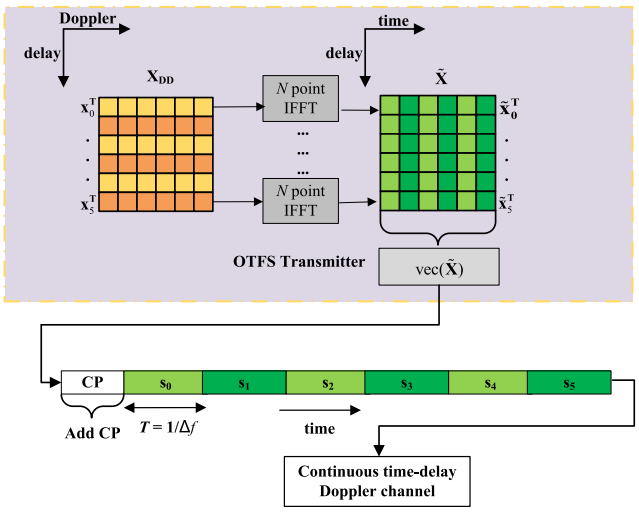

FIGURE 2. OTFS transmitter based on the IDZT using rectangular pulse shaping waveform ($M = 6, N = 6$).

A. TRANSMITTER MODEL

The transceiver system model depicted in Fig. 2 uses inverse discrete Zak transform (IDZT) and OTFS techniques along with rectangular pulse shaping. Let $\mathbf{x} \in \mathbb{C}^{MN\times 1}$ be the transmitted information symbols. The transmitted signal frame has a duration of $T_f = NT$ and a bandwidth of $B = M\Delta f$, where $T\Delta f = 1$, i.e., the OTFS signal is critically sampled

for any pulse-shaping waveform. The information symbols undergo M-QAM modulation, with each symbol having a duration of T_s and occupying a bandwidth of Δf. Mapping these symbols onto a 2D DD domain plane results in the formation of an information symbol matrix $\mathbf{X}_{\mathrm{DD}} \in \mathbb{C}^{M\times N}$. The delay-Doppler plane within the specified region is discretized into a $M \times N$ dimension grid Γ, i.e.,

$$\Gamma = \{(\frac{l}{M\Delta f}, \frac{k}{NT}), l = 0, \cdots, M-1, k = 0, \cdots, N-1\}$$

where $1/M\Delta f$ and $1/NT$ represent the quantization resolutions for the delay and Doppler frequency shift axes, respectively. Meanwhile, M and N denote the number of subcarriers and time slots, respectively. Finally, the data symbols undergo inverse symplectic finite Fourier transform (ISFFT) mapping to represent the information signal $\mathbf{X}_{\mathrm{TF}} \in \mathbb{C}^{M\times N}$ in the time-frequency (TF) domain, i.e.:

$$\mathbf{X}_{\mathrm{TF}} = \mathbf{F}_M \cdot \mathbf{X}_{\mathrm{DD}} \cdot \mathbf{F}_N^H, \tag{1}$$

where $\mathbf{F}_M \in \mathbb{C}^{M\times M}$ and $\mathbf{F}_N^H \in \mathbb{C}^{N\times N}$ denote the Fourier transformation matrix of point M and the inverse Fourier transformation matrix of point N, respectively. The TF domain is obtained by sampling the time and frequency axes at intervals of T seconds and $\Delta f = 1/T$ Hz, respectively. This discretizes the TF signal plane into a $M \times N$ dimension grid Λ, i.e.,

$$\Lambda = \{(m\Delta f, nT), m = 0, \cdots, M-1, n = 0, \cdots, N-1\},$$

where the duration of one symbol is $T = NT_s$. The $\mathbf{X}_{\mathrm{TF}}$ signal is then subjected to a Heisenberg transform to obtain samples in the time-delay domain, Denote:

$$\begin{aligned}\tilde{\mathbf{X}} &= \mathbf{G}_{\mathrm{TX}} \cdot \mathbf{F}_M^H \cdot \mathbf{X}_{\mathrm{TF}} \\ &= \mathbf{G}_{\mathrm{TX}} \cdot \mathbf{F}_M^H \cdot \mathbf{F}_M \cdot \mathbf{X}_{\mathrm{DD}} \cdot \mathbf{F}_N^H \\ &= \mathbf{G}_{\mathrm{TX}} \cdot \mathbf{X}_{\mathrm{DD}} \cdot \mathbf{F}_N^H,\end{aligned} \tag{2}$$

where the waveform of the transmitter pulse is denoted by $\mathbf{G}_{\mathrm{TX}}$. For efficient compatibility with the OFDM modulation system, a rectangular pulse has been considered for the pulse waveform of the transmitter and receiver, i.e., $\mathbf{G}_{\mathrm{TX}} = \mathbf{I}_M$, where $\mathbf{I}_M \in \mathbb{C}^{M\times M}$ is an identity matrix with $M \times M$ dimensions. Wherein (2) in this case also functions as the IDZT. Vectorization of the $\tilde{\mathbf{X}}$ samples yields a time-domain signal of $NM \times 1$ dimensions. i.e., $\mathbf{s} \in \mathbb{C}^{NM\times 1}$.

$$\begin{aligned}\mathbf{s} &= \mathrm{vec}(\tilde{\mathbf{X}}) \\ &= \mathrm{vec}(\mathbf{I}_M \cdot \mathbf{X}_{\mathrm{DD}} \cdot \mathbf{F}_N^H) \\ &= (\mathbf{F}_N^H \otimes \mathbf{I}_M) \cdot \mathrm{vec}(\mathbf{X}_{\mathrm{DD}}),\end{aligned} \tag{3}$$

where vec$(\cdot)$ represent the vectorization operation of a matrix by its column elements, $\otimes$ denote Kronecker product. The time-domain signal is split into N blocks each with M samples, i.e.,$\mathbf{s} = [\,\mathbf{s}_0^{\mathrm{T}}, \mathbf{s}_1^{\mathrm{T}}, \cdots, \mathbf{s}_{N-1}^{\mathrm{T}}]^{\mathrm{T}}$, where $\mathbf{s}_n \in \mathbb{C}^{M\times 1}$, for $n = 0, \cdots, N-1$. A cyclic prefix (CP) is inserted at the beginning of every data frame, with a particular duration T_{CP} and length L_G.

B. CHANNEL MODEL

In a monostatic radar sensing scenario, similar to the [31] system model, the time-varying pulse response of the $P-$tap TF selective sensing channel was modeled as

$$h(t, \tau) = \sum_{p=0}^{P-1} h_p e^{j2\pi \nu_p t} \delta(\tau - \tau_p). \tag{4}$$

In (4), P is the number of paths for scattering and reflection, where the 0-th path is the line of sight path, and h_p is The complex channel gain coefficient that includes the path loss of path components, ν_p and τ_p are the round-trip Doppler shift and round-trip delay shift associated with the propagation $p-$th path, respectively, where $\tau_p \in [0, \frac{1}{\Delta f})$, $\nu_p \in [-\frac{1}{2T}, \frac{1}{2T})$. Moreover, it is possible to distinguish any pair of paths within the DD domain. Each target has a distance R_p and relative velocity for V_p, w.r.t. $p = 0, \cdots, P-1$. V_p has positive and negative bidirectional values. Hence, the following equation is valid:

$$\frac{\tau_p}{2} = \frac{R_p}{c_0}, \frac{\nu_p}{2} = \frac{V_p}{c_0} f_c, \tag{5}$$

where $c_0$and f_c are the speed of light and carrier frequency, respectively. Therefore, the pulse response of the wireless communication channel for OTFS in the DD domain can be given as $h(t, \tau) = \sum_{p=0}^{p=P-1} h_p \delta(\tau - \tau_p)\delta(\nu - \nu_p)$. According to [12], the signal received at the receiving end undergoes down-conversion and discrete sampling and is represented as $\mathbf{r}_{com} = \sum_{p=1}^{P} h_p \Delta^{\kappa_p} \Pi_{MN}^{l_p} \mathbf{s} + \mathbf{w}$, where $\mathbf{r}_{com} \in \mathbb{C}^{NM\times 1}$, $\mathbf{w} \in \mathbb{C}^{NM\times 1}$, $\tau_p = l_p/M\Delta f$, and $\nu_p = \kappa_p/NT$ denotes the normalized delay and normalized Doppler frequency shift, respectively. The communication channel response matrix is expressed by $\mathbf{H}_{com} = \sum_{p=1}^{P} h_p \Delta^{\kappa_p} \Pi_{MN}^{l_p}$ and $\mathbf{H}_{com} \in \mathbb{C}^{MN\times MN}$consisting of the forward-shift circular shift matrix and the diagonal matrix of Doppler frequency shift, i.e.,

$$\begin{aligned}&\Pi_{MN} \in \mathbb{C}^{MN\times MN} \text{and } \Delta \\ &\quad = diag\{e^{j2\pi \frac{0}{MN}}, e^{j2\pi \frac{1}{MN}}, \ldots, e^{j2\pi \frac{MN-1}{MN}}\}.\end{aligned}$$

The additive white Gaussian noise (AWGN) is assumed to be independently and identically distributed, with a zero mean and a variance of $\sigma_w^2 \mathbf{I}_{NM}$, i.e., $\mathbf{w} \sim \mathcal{CN}(0, \sigma_w^2 \mathbf{I}_{NM})$. The above-mentioned channel is in a discrete form. To further estimate the score delay and Doppler shift, we will consider the continuous-delay-and-Doppler-shift (CDDS) radar sensing channel as outlined in [25] and [30]. Then, the received signal can be accordingly written as $\mathbf{r}_{rad} = \sum_{p=1}^{P} h_p \Delta^{\nu_p} \mathbf{s}(\tau_p) \in \mathbb{C}^{MN\times 1}$, where and the expression for the matrix of sampled signals at specific time intervals, given a transmitted signal

with a time delay was derived in [30] as

$$\mathbf{S}_{\tau_p}[l,k] = \begin{cases} \frac{1}{\sqrt{M}} \sum_{m=0}^{M-1} \tilde{X}[m,n] e^{j2\pi m(\frac{l}{M}-\frac{\tau_p}{T})} & l \geqslant l_p \\ \frac{1}{\sqrt{M}} \sum_{m=0}^{M-1} \tilde{X}[m,[n-l_p]_N] e^{j2\pi m(\frac{l}{M}-\frac{\tau_p}{T})} & l < l_p \end{cases}, \tag{6}$$

where $l = 0, 1, \cdots, M-1, k = 0, 1, \cdots N-1$, and $l_p = \lceil \tau_p \cdot M\Delta f \rceil$($\lceil\cdot\rceil$ denote Ceiling function.). $\mathbf{s}_{\tau_p}$ vectorized is $\Pi_{MN}^{l_p}\mathrm{vec}(\Pi_M^{-l}\mathbf{F}_M^H\mathbf{b}(\tau_p)\mathbf{X}_{\mathrm{TF}})$ w.r.t. $\mathbf{b}(\tau_p) = diag\{e^{j2\pi\nu_p 0\Delta f\tau_p}, e^{j2\pi\nu_p 1\Delta f\tau_p}, \cdots, e^{j2\pi\nu_p(M-1)\Delta f\tau_p}\}$. The cyclic shift matrix $\Pi_M^{-l} \in \mathbb{C}^{M\times M}$ can be decomposed by utilizing the eigen-decomposition property of the Fourier transform matrix, giving us a diagonal matrix with $\Pi_M^{-l} = \mathbf{F}_M^H\Lambda\mathbf{F}_M$ as its diagonal elements, where $\Lambda = diag\{e^{j2\pi\frac{l_p}{M}0}, e^{j2\pi\frac{l_p}{M}1}, \cdots, e^{j2\pi\frac{l_p}{M}(M-1)}\} \in \mathbb{C}^{M\times M}$. The $\mathbf{s}(\tau_p)$ can be thus formulated as $\Pi_{MN}^{l_p}(\mathbf{I}_N \otimes (\mathbf{F}_M^H\mathbf{B}(\tau_i)\mathbf{F}_M))\mathbf{s}$, where $\mathbf{B}(\tau_i) = diag\{b^0, b^1, \cdots, b^{M-1}\} \in \mathbb{C}^{M\times M}$ w.r.t. Diagonal matrix $e^{j2\pi(\frac{l_p}{M}-\frac{\tau_p}{T})}$of b. The input-output relationship for the final time-domain baseband signal in the CDDS radar sensing channel can be derived as:

$$\begin{aligned} \mathbf{r}_{rad} &= \sum_{p=1}^{P} h_p \underbrace{\Delta^{\nu_p}\Pi_{MN}^{l_p}(\mathbf{I}_N \otimes (\mathbf{F}_M^H\mathbf{B}(\tau_i)\mathbf{F}_M))}_{\Phi_p}\mathbf{s} + \mathbf{w} \\ &= \underbrace{\sum_{p=1}^{P} h_p\Phi_p}_{\mathbf{G}}\mathbf{s} + \mathbf{w} \\ &= \mathbf{G}\mathbf{s} + \mathbf{w}. \end{aligned} \tag{7}$$

where $\Phi_p \in \mathbb{C}^{NM\times NM}$and $\mathbf{G} \in \mathbb{C}^{NM\times NM}$

C. RECEIVER MODEL

The OTFS receiver model based on discrete Zak transform (DZT) and rectangular pulse shaping is illustrated in Fig. 3. At the receiving end, the signal is received as a protected and isolated discrete signal with dimensions of $NM \times 1$, which are defined as the specific signal received without additional information on its components, i.e., $\mathbf{r}_{rad} \in \mathbb{C}^{NM\times 1}$, where $\mathbf{r} = [\mathbf{r}_0^{\mathrm{T}}, \mathbf{r}_1^{\mathrm{T}}, \cdots, \mathbf{r}_{N-1}^{\mathrm{T}}]^{\mathrm{T}}$, for $n = 0, \cdots, N-1$. Then, convert $\mathbf{r}$into a delay-time domain signal matrix $\tilde{\mathbf{Y}} \in \mathbb{C}^{M\times N}$, i.e., $\tilde{\mathbf{Y}} = \mathbf{G}_{\mathrm{RX}} \cdot (\mathrm{vec}_{M,N}^{-1}(\mathbf{r}_{rad}))$.$\mathrm{vec}_{M,N}^{-1}(\cdot)$ operation is a matrix formed by folding a vector into an $M-$by$-N$ matrix by filling it column-wise. To ensure compatibility with the OFDM system, i.e., $\mathbf{G}_{\mathrm{RX}} = \mathbf{I}_M$. It follows that the Wigner transform is applied to convert the $\tilde{\mathbf{Y}}$ matrix $\mathbf{Y}_{\mathrm{TF}} \in \mathbb{C}^{M\times N}$ to the TF domain, i.e., $\mathbf{Y}_{\mathrm{TF}} = \mathbf{F}_M \cdot \tilde{\mathbf{Y}}$. Subsequently, the $\mathbf{Y}_{\mathrm{TF}}$ can be transformed into the DD domain signal matrix $\mathbf{Y}_{\mathrm{DD}} \in \mathbb{C}^{M\times N}$using the symplectic finite Fourier transform (SFFT) transformation. It then follows that DZT is givens by

$$\mathbf{Y}_{\mathrm{DD}} = \mathbf{F}_M^H \cdot \mathbf{Y}_{\mathrm{TF}} \cdot \mathbf{F}_N = \mathbf{F}_M^H \cdot \mathbf{F}_M \cdot \tilde{\mathbf{Y}} \cdot \mathbf{F}_N = \tilde{\mathbf{Y}} \cdot \mathbf{F}_N. \tag{8}$$

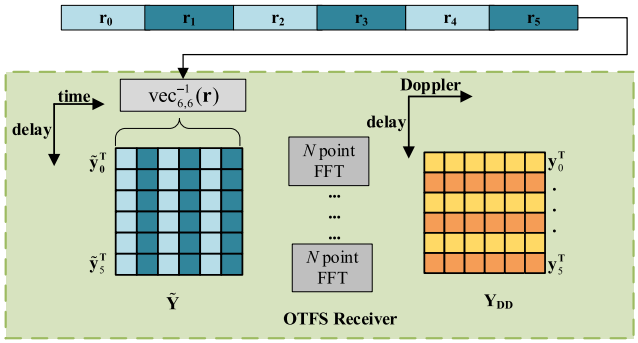

FIGURE 3. OTFS receiver based on the DZT using rectangular pulse shaping waveform (M= 6, N = 6).

The matrix $\mathbf{Y}_{\mathrm{DD}}$ contains the DD samples which are vectorized to obtain the DD samples $\mathbf{y} \in \mathbb{C}^{MN\times 1}$, i.e., $\mathbf{y} = \mathrm{vec}(\mathbf{Y}_{\mathrm{DD}}) \in \mathbb{C}^{MN\times 1}$.which are given by

$$\mathbf{y} = \mathbf{H}_{\mathrm{DD}}\mathbf{x} + \tilde{\mathbf{w}}, \tag{9}$$

where $\tilde{\mathbf{w}} = (\mathbf{F}_N \otimes \mathbf{I}_M)\mathbf{w} \in \mathbb{C}^{NM\times 1}$, i.e., $\tilde{\mathbf{w}} \sim \mathcal{CN}(0, \sigma_w^2\mathbf{I}_{NM})$. The relationship between the time domain channel and DD domain channel matrix can be derived from (7) and (9) as follows:

$$\begin{aligned} \mathbf{H}_{\mathrm{DD}} &= (\mathbf{F}_N \otimes \mathbf{I}_M)\mathbf{G}(\mathbf{F}_N^H \otimes \mathbf{I}_M) \\ &= \sum_{p=1}^{P} h_p\mathbf{\Psi}_p(\tau_p, \nu_p), \end{aligned} \tag{10}$$

where $\mathbf{\Psi}_p(\tau_p, \nu_p) \triangleq (\mathbf{F}_N \otimes \mathbf{I}_M)\Phi_p(\mathbf{F}_N^H \otimes \mathbf{I}_M) \in \mathbb{C}^{MN\times MN}$

III. ESTIMATION OF TARGET PARAMETERS

A. MAXIMUM LIKELIHOOD ESTIMATOR

Sensing aims to estimate target parameters, including time delay and Doppler frequency shift sets$\{(\tau_p, \nu_p)\}$, which can be utilized to calculate the distance and velocity of a target. The estimation of 3P parameters is required for P targets, which means estimating P sets of channel coefficients, time delay shift, and Doppler frequency shift parameters. This refers to the maximum likelihood estimation of 3P sets of unknown parameters $\hat{\boldsymbol{\theta}} = \{\hat{h}_1, , \cdots, \hat{h}_P, \hat{\tau}_1, \cdots, \hat{\tau}_P, \hat{\nu}_1, \cdots, \hat{\nu}_P\}$. Through (10), a channel matrix containing parameter dependency relationships can be obtained. In a monostaticradar sensingscenario, the symbol sent at the radar detector is known, which allows for the derivation of the likelihood function $l(\mathbf{y}|\boldsymbol{\theta}, \mathbf{x})$, yielding

$$\begin{aligned} l(\mathbf{y}|\boldsymbol{\theta}, \mathbf{x}) &= \|\mathbf{y} - \mathbf{H}_{DD}\mathbf{x}\|^2 \\ &= \left\| \mathbf{y} - \sum_{p=1}^{P} h_p\mathbf{\Psi}_p\mathbf{x} \right\|^2, \end{aligned} \tag{11}$$

where $\|\cdot\|$ denote 2-Norm operation. We can obtain (12) for MLE as follows:

$$\hat{\boldsymbol{\theta}} = (\hat{h}_p, \hat{\tau}_p, \hat{\nu}_p) = \arg \min_{\theta \in \mathbb{C}^P \times \mathbb{R}_+^P \times \mathbb{R}^P} \left\| \mathbf{y} - \sum_{p=1}^{P} h_p \boldsymbol{\Psi}_p \mathbf{x} \right\|^2. \tag{12}$$

Attempting to search for the optimal solution in the continuous 3P dimension would thereby make it infeasible, as the complexity would demonstrate exponential growth. Therefore, we propose the MF-F method to achieve a less complex approximation of the ML solution. The channel's gain coefficient is characterized by a quadratic constant pattern for a specific arrangement of parameters $\{(\tau_p, \nu_p)\}$in (11). Hence, resolving $\{h_p\}$before implementing the MLE approach to evaluate the remaining parameters. This approach facilitates the transformation of the search estimation from a 3P-dimensional to a 2P-dimensional space. Afterward, we apply the circular shifting property of the unitary circulant matrix to (12) to perform a rough integer parameter estimation within the grid range using the matching filter algorithm. Subsequently, we use the Fibonacci algorithm to perform off-grid search. The Fibonacci search concept involves using the index value corresponding to the Fibonacci sequence in a sorted array to determine the range for the subsequent search. Compared to other search techniques, Fibonacci search is more versatile and can be applied to any data structure.

B. PROPOSED MF-F PARAMETERS ESTIMATION ALGORITHM

In the event of a solitary estimation target, i.e., $P = 1$. According to (12), we can derive the maximization problem by obtaining $\hat{h} = \frac{(\boldsymbol{\Psi x})^H \cdot \mathbf{y}}{\|\boldsymbol{\Psi x}\|^2}$ and (13). The derivation process for (11)-(13) and $\hat{h}$ is given in Appendix A.

$$(\hat{\tau}, \hat{\nu}) = \arg \max_{(\hat{\tau}, \hat{\nu})} \left| (\boldsymbol{\Psi x})^H \cdot \mathbf{y} \right|^2. \tag{13}$$

As we extend from a single-target scenario to multiple targets, potential interference among different targets must be taken into consideration. Specifically, when estimating the $p-$th target, the remaining p-1 targets can significantly interfere, as expressed by

$$\mathbf{y} = \underbrace{h_p \boldsymbol{\Psi}_p(\tau_p, \nu_p)\mathbf{x}}_{Useful\ Signal} + \underbrace{\sum_{q \neq p}^{P} h_q \boldsymbol{\Psi}_q(\tau_q, \nu_q)\mathbf{x}}_{ISI\ Interference\ Signal} + \tilde{\mathbf{w}}. \tag{14}$$

The $p-$th target under current estimation is considered a useful signal $h_p \boldsymbol{\Psi}_p(\tau_p, \nu_p)\mathbf{x}$, whereas the remaining P-1 target signals $\sum_{q \neq p}^{P} h_q \boldsymbol{\Psi}_q(\tau_q, \nu_q)\mathbf{x}$ are deemed useless due to their interference with the estimation of the targets mentioned above. To minimize interference during parameter estimation of the $p-$th target, interference signals in the estimated p-1 targets must be removed, optimizing the effect

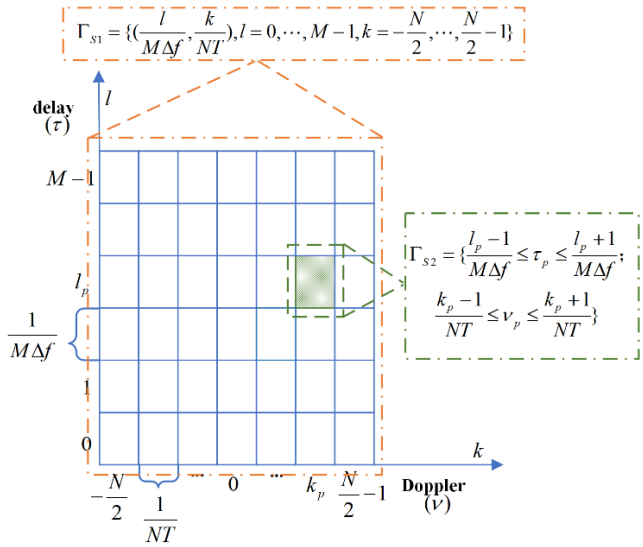

FIGURE 4. Two search areas Γ_{s1} and Γ_{s2}, respectively.

of interference cancellation, which is

$$\mathbf{y}_p = \mathbf{y} - \sum_{q=2}^{p-1} h_q \boldsymbol{\Psi}_q(\tau_q, \nu_q)\mathbf{x}\ 1 \leqslant q \leqslant p, \tag{15}$$

for $q = 1, \cdots, p-1$and $p = 2, \cdots, P$. Combining the single-target channel gain coefficient $\hat{h}_p$can be deduced by

$$\hat{h}_p = \begin{cases} \dfrac{(\Psi_p(\tau_p, \nu_p) \cdot x)^H \cdot y}{\left\| \Psi_p(\tau_p, \nu_p) \cdot x \right\|^2} p = 1 \\ \dfrac{(\Psi_p(\tau_p, \nu_p) \cdot x)^H \cdot y_p}{\left\| \Psi_p(\tau_p, \nu_p) \cdot x \right\|^2} p > 2 \end{cases}, \tag{16}$$

where $\tau_p \in [0, \frac{1}{\Delta f})$ and $\nu_p = [-\frac{1}{2T}, \frac{1}{2T})$ represent the search interval of MLE in $\mathbb{R}_+^P \times \mathbb{R}^P$ dimensions. This study proposes an approach to partitioning an area into two regions aiming to estimate parameters, thus, reducing uncertainty and enhancing accuracy. Let us denotes these regions as region Γ_{S1} and region Γ_{S2}, respectively, as shown in Fig. 4. Region $\boldsymbol{\Gamma}_{\mathbf{s1}} = \{ \left(\frac{l}{M\Delta f}, \frac{k}{NT} \right), l = 0, \cdots, M-1, k = -\frac{N}{2}, \cdots, \frac{N}{2}-1$ is estimated to be integer parameters in the DD domain; The second area $\boldsymbol{\Gamma}_{\mathbf{s2}} = \{ (\tau_p, \nu_p), \frac{\hat{l}-1}{M\Delta f} \le \tau_p \le \frac{\hat{l}+1}{M\Delta f}, \frac{\hat{k}-1}{NT} \le \nu_p \le \frac{\hat{k}+1}{NT}$ is designated for estimating parameter fractions.

The estimation of MF-F parameters comprises two stages, In the first stage, the rough estimates of the parameters are obtained by matching filter parameter estimation. The second stage involves using the Fibonacci method for refined parameter estimation.

1) *Estimation of the step parameters for the MF*: The delay and Doppler resolution are currently integer multiples of each other. i.e., $l_p = \left\lceil \frac{\tau_p}{\frac{1}{M\Delta f}} \right\rceil$ and $\kappa_p = \left\lceil \frac{\nu_p}{\frac{1}{NT}} \right\rceil$. The input-output relationship of the information symbol matrices in the DD domain, for the reduced cyclic prefix (RCP) modulation

variant of OTFS in [16], is approximately represented by a circular shift of the transmitted symbol and it is given by

$$\mathbf{Y}_{\mathrm{DD}}[l,k]=\sum_{p=1}^{P}h_p\alpha_{l_p,\kappa_p}[l,k]\cdot\mathbf{X}_{\mathrm{DD}}[[l-l_p]_M,[k-\kappa_p]_N]+\mathbf{W}[l,k],\quad(17)$$

where

$$\alpha_{l_p,\kappa_p}[l,k]=\begin{cases}e^{j\frac{2\pi}{MN}\kappa_p(l-l_p)} & l_p\leqslant l<M\\ e^{j\frac{2\pi}{MN}\kappa_p([l-l_p]_M)}e^{j2\pi n/N} & 0\leqslant l<l_p\end{cases}$$

and $\mathbf{W}[l,k]\sim\mathcal{CN}(0,\Sigma_w)$ denotes the AWGN with zero mean covariance matrix Σ_w, and can be concisely written as

$$\begin{aligned}\mathrm{vec}(\mathbf{Y})&=\mathrm{vec}(\sum_{p=1}^{P}\beta_p\Pi_M^{l_p}\mathbf{X}_{\mathrm{DD}}\Pi_N^{-\kappa_p}+\mathbf{I}_{ISI}+\mathbf{W})\\ \mathbf{y}&=\underbrace{\beta\mathrm{vec}(\Pi_M^{l_p}\mathbf{X}_{\mathrm{DD}}\Pi_N^{-\kappa_p})}_{Useful\ Signal}+\underbrace{\mathrm{vec}(\mathbf{I}_{ISI})}_{ISI\ Interference\ Signal}+\mathrm{vec}(\mathbf{W}).\end{aligned}\quad(18)$$

In (18) $\mathbf{Y}\in\mathbb{C}^{M\times N}$, $\mathbf{y}\in\mathbb{C}^{MN\times 1}$, $\beta_p=h_p\alpha_{l_p,\kappa_p}[l,k]$, $\Pi_M^{l_p}\mathbf{X}_{\mathrm{DD}}\Pi_N^{-\kappa_p}\in\mathbb{C}^{M\times N}$. The useful signal $\beta\mathrm{vec}(\Pi_M^{l_p}\mathbf{X}_{\mathrm{DD}}\Pi_N^{-\kappa_p})$ and the interference $\mathrm{vec}(\mathbf{I}_{ISI})$ term correspond respectively to the two terms in (14). If multiple targets are present, one can obtain interference-free receiving signals by utilizing (15); otherwise, the receiving signals can be acquired without interference. The complex channel coefficients can be derived from (16). Subsequently, the obtained values are substituted into (13) to solve the maximization problem, which is

$$(\hat{l}_p,\hat{\kappa}_p)=\arg\max_{(\hat{l}_p,\hat{\kappa}_p)}\left|\mathrm{vec}(\Pi_M^{l_p}\mathbf{X}_{\mathrm{DD}}\Pi_N^{-\kappa_p})^H\cdot\mathbf{y}_p\right|^2.\quad(19)$$

At this juncture, we have determined the upper and lower limits of the fraction estimation, i.e., Γ_{S2}area.

2) *Refinement estimation of F-step parameters:* The process of conducting the off-grid search in Γ_{S2} area can be given similarly to (19) as

$$(\hat{\tau}_p,\hat{\nu}_p)=\arg\max_{(\hat{\tau}_p,\hat{\nu}_p)\in\Gamma_{s2}}\left|(\mathbf{\Psi}_p\mathbf{x})^H\cdot\mathbf{y}_p\right|^2.\quad(20)$$

We propose a 2D Fibonacci method to solve the maximization problem in 2D. The Fibonacci search method is a divide-and-conquer algorithm utilized to search for sorted arrays. The application of Fibonacci numbers enables the narrowing down of possible locations and decreases uncertainty [32]. In a binary search, the sorted array is partitioned in half, and one of the two partitions is selected for further examination. This technique is also known as the half-interval search method. Fibonacci search differs from binary search by dividing the array into two parts using a contiguous Fibonacci sequence. This results in an increase of approximately 4% in the number of comparisons performed [33]. The average and worst-case complexities of the Fibonacci search algorithm are both $\mathcal{O}(\log(n))$. The Fibonacci search method has several properties: *a)* The Fibonacci method and golden section method have the same interval reduction rate as n approaches infinity, resulting in linear convergence to the convergence ratio of 0.618 for the Fibonacci method. Hence, the Fibonacci method converges linearly to a 0.618 convergence ratio. *b)* The optimal strategy for solving one-dimensional minimization problems using the division method is the Fibonacci method, while the golden section method is an approximative optimal one. *c)* Prior knowledge of the number of calculations needed to evaluate the function and the Fibonacci series is required for the Fibonacci method. This approach reduces the interval of uncertainty at each step using the Fibonacci series.

The distance and velocity of the target can be calculated using the estimated delay and Doppler, as shown (5), i.e., $R_p=\hat{\tau}_pc_0/2$, and $V_p=\hat{\nu}_pc_0/2f_c$. For multi-target estimation, interference signals from the p-1 targets are eliminated when estimating the parameters of the $p-$th target. Each target estimation is divided into two stages. In the first stage, the integer parts of the delay and Doppler parameters are estimated using (19) to reduce the search area in the second stage. In the second stage, fractional delay and Doppler shift parameters are estimated using the 2D Fibonacci search method and (20), and the complex channel coefficient parameters are updated according to (16).

C. PERFORMANCE BOUNDS

The Cramér-Rao lower bound (CRLB) provides a lower bound on the variance of unbiased estimators of deterministic parameters. It is a measure that can be used to describe the performance limits of OTFS systems. Previous work has analyzed the system limits from the perspective of CRLB, including [25] and [34]. More recently, [35] summarized the CRLB of four types of waveform systems and showed through both CRLB deduction and numerical analysis that the OTFS has superior sensing performance to OFDM at the same bandwidth. The waveform system utilized in this paper conforms to the two-step OTFS system described in [35]. To ensure compatibility with existing OFDM systems, the OTFS receiver performs a two-step conversion. Specifically, it first uses an OFDM demodulator to transform the received time-domain signal to the time-frequency domain and then channels the TF signal through the SFFT transform to the DD domain. We demonstrate the CRLB of the waveform system used in this paper by applying algebraic operations to (17), yielding (21). We refer readers to [25] and [35] for further details.

$$\mathbf{Y}_{\mathrm{DD}}[l,k]=\sum_{k'=0}^{N-1}\sum_{l'=0}^{M-1}\sum_{p=1}^{P}\mathbf{\Psi}_{k,k'}^{p}[l,l']\mathbf{X}_{\mathrm{DD}}[l,k],\quad(21)$$

where $\mathbf{\Psi}^p_{k,k'}[l,l'] \in \mathbb{C}^{M\times M}$, which is

$$\mathbf{\Psi}^p_{k,k'} = \begin{bmatrix} \Psi^{\,p}_{k,k'}[0,M-1] & \cdots & \Psi^{\,p}_{k,k'}[0,M-1] \\ \vdots & \ddots & \vdots \\ \Psi^{\,p}_{k,k'}[0,M-1] & \cdots & \Psi^p_{k,k'}[0,M-1] \end{bmatrix} \tag{22}$$

and the matrix expression is given by

$$\begin{aligned}\mathbf{\Psi}^p_{k,k'}[l,l'] = &\frac{1}{MN} h_p e^{j2\pi\kappa_p l_p} \mathrm{Dir}(\kappa_p NT - k + k', N) \\ &\cdot \mathrm{Dir}(l - l_p M\Delta f - l', M) e^{j2\pi\kappa_p \frac{l'}{M\Delta f}} \\ &\cdot \begin{cases} 1 \; l_p \leqslant l < M \\ e^{-j2\pi(\kappa_p T + \frac{k'}{N})} \; 0 \leqslant l < l_p \end{cases}.\end{aligned} \tag{23}$$

where the $\mathrm{Dir}(\varphi, Z) = \sum_z^{Z-1} e^{j2\pi\varphi\frac{z}{Z}}$ is Dirichlet kernel function, when k is a multiple of Z, the function evaluates to Z or -Z, depending on whether Z is even or odd. In contrast, for all other integer values that are not φ, it is equal to zero, making it very distinct from other kernel functions. Consequently, the channel matrix $\mathbf{\Psi}^p$ can be expressed as

$$\mathbf{\Psi}^p = \begin{bmatrix} \mathbf{\Psi}^p_{0,0} & \cdots & \mathbf{\Psi}^p_{0,N-1} \\ \vdots & \ddots & \vdots \\ \mathbf{\Psi}^p_{0,0} & \cdots & \mathbf{\Psi}^p_{0,N-1} \end{bmatrix}. \tag{24}$$

The derivatives of $\mathbf{\Psi}^p_{k,k'}[l,l']$ in (24) w.r.t κ_p and l_p can be obtained as

$$\begin{aligned}\frac{\partial \mathbf{\Psi}^p_{k,k'}[l,l']}{\partial(l_p)} = &\frac{j2\pi}{MN} h_p \mathrm{Dir}(\kappa_p NT - k + k', N) e^{j2\pi\kappa_p \frac{l'}{M\Delta f}} \\ &\cdot \sum_{m=0}^{M-1} (\kappa_p - M\Delta f) e^{j2\pi(l - l_p M\Delta f - l')\frac{m}{M}} \\ &\cdot \begin{cases} 1 \; l_p \leqslant l < M \\ e^{-j2\pi(\kappa_p T + \frac{k'}{N})} \; 0 \leqslant l < l_p \end{cases},\end{aligned} \tag{25}$$

$$\begin{aligned}\frac{\partial \mathbf{\Psi}^p_{k,k'}[l,l']}{\partial(\kappa_p)} = &\frac{j2\pi}{MN} h_p (l - l_p M\Delta f - l', M) e^{j2\pi\kappa_p (l_p + \frac{l'}{M\Delta f})} \\ &\cdot \sum_{n=0}^{N-1} e^{j2\pi(\kappa_p NT - k + k')\frac{n}{N}} \\ &\cdot \begin{cases} l_p + nT + \dfrac{l'}{M\Delta f} \; l_p \leqslant l < M \\ l_p + n - 1T + \dfrac{l'}{M\Delta f} e^{-j2\pi(\kappa_p T + \frac{k'}{N})} \; 0 \leqslant l < l_p \end{cases}.\end{aligned} \tag{26}$$

Next, we use the derived partial derivatives to obtain the Fisher Information Matrix (FIM). According to [36], FIM is a measure of the information an observed data point provides about an unknown parameter.

$$\mathbf{J}(\theta) = \mathbb{E}\left\{ [\frac{\partial}{\partial\boldsymbol{\theta}} \log l(\mathbf{y}|\boldsymbol{\theta}, \mathbf{x})][\frac{\partial}{\partial\boldsymbol{\theta}} \log l(\mathbf{y}|\boldsymbol{\theta}, \mathbf{x})]^{\mathrm{T}} \right\}. \tag{27}$$

Assuming that the received signal interferes with additive Gaussian white noise $\mathbf{N} \sim \mathcal{CN}(0, \Sigma_N)$, where $\Sigma_N$is the covariance matrix in this study, we extended the scenario presented in Appendix A to high-dimensional cases, i.e., $\mathbf{y} \sim \mathcal{CN}(0, \Sigma_N)$, where can be obtained as the logarithmic probability function $\mathbf{y}$w.r.t. $\boldsymbol{\theta}$, we get

$$f(\mathbf{y};\boldsymbol{\theta}) = \log l(\mathbf{y}|\boldsymbol{\theta}, \mathbf{x}) = -(\mathbf{y} - \mathbf{\Psi}\boldsymbol{x})^H \Sigma^{-1} (\mathbf{y} - \mathbf{\Psi}\boldsymbol{x}). \tag{28}$$

The derivatives of $f(\mathbf{y};\boldsymbol{\theta})$in (28) w.r.t. $\boldsymbol{\theta}$, which is

$$\begin{aligned}\frac{\partial}{\partial\boldsymbol{\theta}_i} f(\mathbf{y};\boldsymbol{\theta}_i) = &-(\mathbf{y} - \mathbf{\Psi}\boldsymbol{x})^H \Sigma^{-1} \frac{\partial\mathbf{\Psi}}{\partial\boldsymbol{\theta}_i}\mathbf{x} \\ &- (\frac{\partial\mathbf{\Psi}}{\partial\boldsymbol{\theta}_i}\mathbf{x})^H \Sigma^{-1} (\mathbf{y} - \mathbf{\Psi}\boldsymbol{x}),\end{aligned} \tag{29}$$

The second derivative is taken to obtain the (30), and its expected value is computed. The resulting expression is as follows

$$\mathbb{E}\left\{ \frac{\partial^2}{\partial\boldsymbol{\theta}_i \partial\boldsymbol{\theta}_j} f(\mathbf{y};\boldsymbol{\theta}_i) \right\} = -2\Re\left\{ (\frac{\partial\mathbf{\Psi}}{\partial\boldsymbol{\theta}_j}\mathbf{x})^H \Sigma^{-1} \frac{\partial\mathbf{\Psi}}{\partial\boldsymbol{\theta}_i}\mathbf{x} \right\}, \tag{30}$$

Thus, FIM can be obtained as

$$\mathbf{J}(\theta) = [\mathrm{J}_{i,j}]_{1\leqslant i,j\leqslant 3P}, \tag{31}$$

where $\mathrm{J}_{i,j} = -\mathbb{E}(\frac{\partial^2 f(\mathbf{y};\boldsymbol{\theta}_i)}{\partial\boldsymbol{\theta}_i \partial\boldsymbol{\theta}_j^*})$. The mean square error (MSE) of an unbiased estimator satisfies:

$$\mathbf{E}\left\{ (\hat{\boldsymbol{\theta}} - \boldsymbol{\theta})(\hat{\boldsymbol{\theta}} - \boldsymbol{\theta})^T \right\} \boldsymbol{J}^{-1}(\theta). \tag{32}$$

The $\mathbf{J}^{-1}(\theta)$ main diagonal elements represent the expected CRLB of the unknown estimated parameters. Supplemental information regarding the CRLB for OFDM and when using the ZAK transform, rather than the two-stage transformed OTFS waveform described in this paper, may be found in [35].

IV. NUMERICAL RESULTS AND DISCUSSION

This section aims to validate the reliability of the proposed MF-F algorithm by analyzing the curve distribution map and estimation results under both the single and multiple targets. Next, we evaluate the accuracy and robustness of the MF-F method by analyzing the Root Mean Squared Error (RMSE) under different signal-to-noise ratios (SNR). The evaluation of RMSE is also conducted with different numbers of targets. Then, the effectiveness of the proposed algorithm is established by comparing the parameter estimation results of different algorithms, particularly regarding a single target. Finally, using a software-defined radio (SDR) platform, a simple ISAC system was constructed to evaluate the performance of the proposed algorithm in practical scenarios. The simulation parameters of the OTFS waveform are listed in TABLE 1.

To evaluate the accuracy and ambiguity of the perception algorithm for target recognition, we present a 2D normalized profile map of velocity and range with varying numbers of

(a) (b)

FIGURE 5. The 2D range-velocity profile for a rough estimation. (a) The single target rough estimation of normalized distribution; (b) The multiple targets rough estimation of normalized distribution.

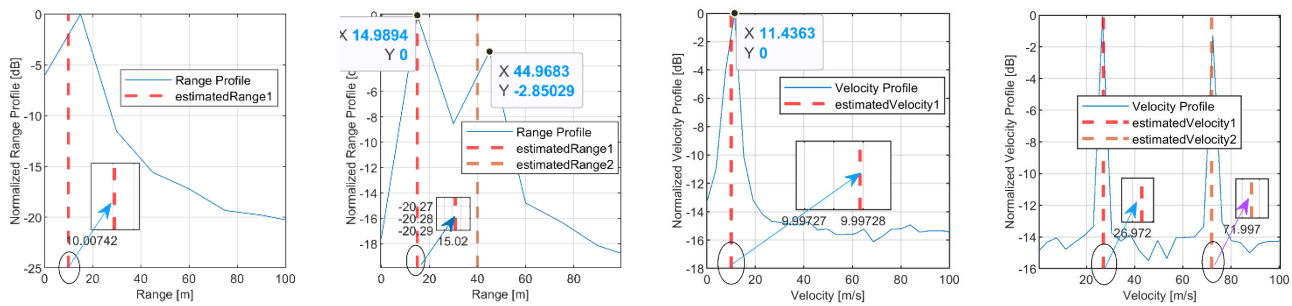

(a) (b) (c) (d)

FIGURE 6. Normalized curves for range and velocity estimation. (a) Single target coarse estimation vs refined estimation distance; (b) Multiple targets coarse estimation vs refined estimation distance; (c) Single target coarse estimation vs refined estimation velocity; (d) Multiple targets coarse estimation vs refined estimation velocity.

TABLE 1. Simulation parameters.

Symbol	Parameter	Value
f_c	Carrier frequency	24 GHz
N_c	Number of subcarriers	256
B	Total signal bandwidth	10 MHz
Δf	Subcarriers spacing	39.063 KHz
N_s	Number of symbols (time slots)	64
M	Symbol modulation order	4
ΔR	Range resolution	15 m
ΔV	Velocity resolution	3.8125 m/s
R_{max}	Unambiguous range	3840 m
V_{max}	Unambiguous velocity	±122 m/s
SNR	Signal-to-noise ratio	10 dB

targets under the rough estimation results of the MF step. On this graph, the normalized amplitude has an enormous value only in specific regions, where the maximum values correspond to the estimated velocity and range of the targets. Ultimately, the results of super-resolution estimation are presented. TABLE 2 provides a framework for setting the estimated parameters. The parameter set for the single target estimated range-velocity pair is $\{(\mathrm{R}_1 = 10\ \mathrm{m}, \mathrm{V}_1 = 10\ \mathrm{m/s})\}$, while for multiple targets, range and velocity parameters are set $\{(R_1 = 15\ \mathrm{m}, \mathrm{V}_1 = 27\ m/s)\}$ and $\{(\mathrm{R}_2 = 40\ \mathrm{m}, \mathrm{V}_2 = 72\ \mathrm{m/s})\}$. separately. As shown in Fig. 5(a)-(b), a rough estimation of the normalized profile of perceived results for velocity and range is given. TABLE 2 shows the range-velocity values estimates for Fig. 5(a)-(b), which display one and two peaks, respectively. Although there is a significant difference between the estimated and actual distance values, the deviation of the estimated speed values is relatively minor. Nevertheless, despite the deviation of the estimated value, it can accurately determine the number of targets and reduce the search range for F-step super-resolution estimation.

To verify the accuracy of the F-step refined estimation algorithm and compare it to the MF-step coarse estimation results, normalized curves of range and velocity coarse estimates were illustrated under different conditions in Fig. 6(a)-(d). Additionally, the estimated super-resolution values were represented by dashed lines. The results revealed

TABLE 2. Target parameters set and estimated parameters values.

Number of Targets	Actual Range-Velocity Pairs	Rough Estimate of Range -Velocity Pairs	Refined Estimation of Range -Velocity Pairs
Single Target	{R_1=10 m, V_1=10 m/s}	{R_1=14.989 m, V_1=11.436 m/s}	{R_1=10.007 m, V_1=9.997 m/s}
Multiple Targets	{R_1=15 m, V_1=27 m/s}	{R_1=14.989 m, V_1=26.684 m/s}	{R_1=15.020 m, V_1=26.972m/s}
	{R_2=40 m, V_2=72 m/s}	{R_2=44.968 m, V_2=72.43 m/s}	{R_2=39.991 m, V_2=71.997 m/s}

that the deviation between the estimated super-resolution values and the actual values for distance and speed is negligible. According to TABLE 2, the maximum deviation for distance estimation and velocity estimation is 0.02 m and 0.028 m/s, respectively.

To assess the accuracy of the proposed algorithm without bias, Monte Carlo simulation experiments were conducted. To measure performance, the RMSE was used as the metric for sensing accuracy. We assume that there exist scenarios with 1, 2, and 3 targets, respectively, i.e., $p = 1, 2, 3$. The simulation parameters remain unchanged as presented in Table 1, except for the SNR which is uniformly distributed between -20 dB and 20 dB. The estimated parameters of the targets are set for$\{(R_1 = 5\text{ m}, V_1 = 10\text{m/s})\}$, $\{(R_2 = 20\text{ m}, V_2 = 20\text{m/s})\}$, and$\{(R_3 = 60\text{ m}, V_3 = 40\text{m/s})\}$, respectively. The RMSE is used to calculate the error between distance and velocity, i.e., $\text{RMSE} = \left(\frac{1}{N}\sum_{i=1}^{N}(x_i - \hat{x}_i)^2\right)^{1/2}$ w.r.t. x_i is a value in the set of true values and $\hat{x}_i$ is the corresponding estimated value in the set. The proposed MF-F algorithm is employed to perform 100 Monte Carlo simulations for each target, and the resulting RMSE values are compared and characterized in Figs. 7-8 shows the accuracy comparison of velocity and range estimation, respectively. The curve in Fig. 7 indicates that for a single target scenario, when the SNR is 10 dB, the RMSE of velocity estimation approaches 10^{-3} m/s, which suggests high accuracy in millimeter-per-second level estimation. On the other hand, in the presence of multiple targets and low SNR of 0 dB, the curve in the figure suggests that the RMSE approximates 10^{-2} m/s. This implies that the accuracy of estimating velocity is at the centimeter-per-second level. In Fig. 8, the distance estimation RMSE of the system is displayed. For single-target scenarios, at an SNR of 5 dB, the estimate reaches 10^{-2} m. At an SNR of 15 dB, the RMSE drops to less than 10^{-3}m, demonstrating millimeter-level accuracy. In the case of multiple targets, the RMSE equals 10^{-1}m at which point the SNR declines to -5 dB. An observation can be made from the distribution trends of the three distinct curves indicating different target numbers depicted in Figs. 7-8. The RMSE value is seen to be progressively increasing with an increase in the P value.

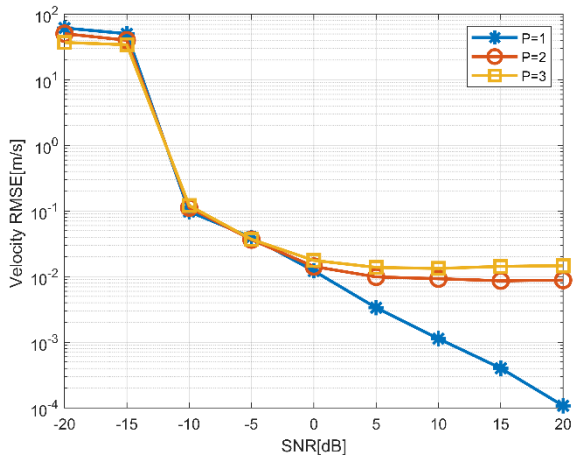

FIGURE 7. RMSE vs velocity based on different numbers of targets.

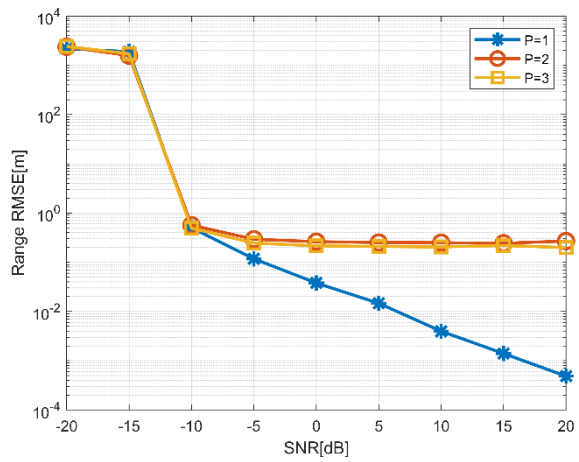

FIGURE 8. RMSE vs range based on different numbers of targets.

Hence, it can be stated that the number of targets has a noteworthy impact on perceptual accuracy. The reason for this impact is that the estimation of the current target is influenced by interference from other targets. As the SNR increases, the RMSE values for multiple targets converge to a stable value. e.g., in velocity perception, the stable value is 0 dB, which corresponds to a convergence of RMSE to 10^{-2} m/s; In comparison, in distance perception, the RMSE approaches 10^{-1} m as the SNR becomes -5 dB.

To explicitly illustrate the effectiveness of the proposed MF-F algorithm, we undertook a thorough comparative analysis against established algorithms, specifically the MF algorithm [28], the FFT algorithm [19], the FCCC algorithm in [20], and the MUSIC algorithm [17]. TABLE 3 indicates the simulation parameters that were configured following the settings provided in [22]. The simulation was conducted to run 100 Monte Carlo experiments for each algorithm with estimated parameters set at $\{(R_1 = 10\text{ m}, V_1 = 36\text{km/h})\}$ and$\{(R_2 = 30\text{ m}, V_1 = 320\text{km/h})\}$, respectively. The results as showcased in Figs. 9-10. we see in Fig. 9 that the

TABLE 3. Simulation parameters for different algorithms.

Symbol	Parameter	Value
f_c	Carrier frequency	2 GHz
N_c	Number of subcarriers	64
B	Total signal bandwidth	320 MHz
Δf	Subcarriers spacing	5 KHz
N_s	Number of symbols (time slots)	16
M	Symbol modulation order	4
SNR	Signal-to-noise ratio	-40~40 dB

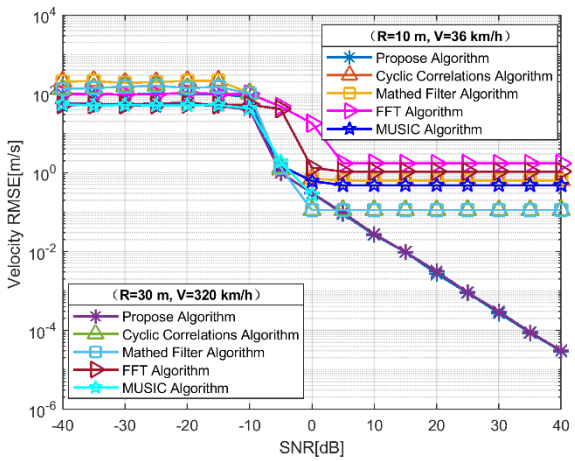

FIGURE 9. RMSE vs velocity for various algorithms.

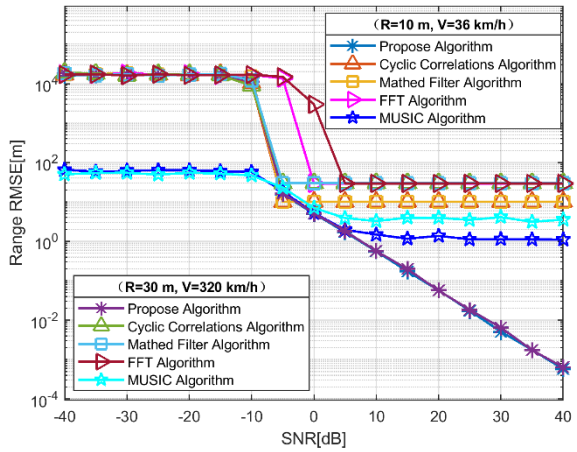

FIGURE 10. RMSE vs range for various algorithms.

MF-F algorithm proposed in this study exhibits superior speed-sensing performance compared to other algorithms. Conversely, the FFT algorithm exhibits the worst speed-sensing performance out of all the algorithms. In contrast, the performance of the FCCC and MF algorithms is comparable regarding speed sensing. Fig. 10 shows the range-sensing RMSE profile at 5 dB SNR, the RMSE values of other algorithms are higher than those of the MF-F algorithm, indicating the latter superior perceptual accuracy. Additionally, the perceptual RMSE value of the proposed MF-F algorithm remains stable under varying conditions, demonstrating its robustness, while other algorithms become unstable, signifying their lack of robustness. The above-mentioned results demonstrate the effectiveness of the proposed MF-F algorithm. Furthermore, by considering the simulation results under different conditions shown in Figs. 7-8, it is evident that the MF-F algorithm proposed in this work possesses robustness.

The paper provides a complexity analysis of the MF-F algorithm, which is split into two parts. The first part involves the MF step, which uses (19). This step includes a low-complexity $\mathcal{O}(M) + \mathcal{O}(N)$circular shift operation involving a complexity $\mathcal{O}(MN)$of as well as a multiplication operation. The second part, i.e., the F step entails a computational complexity $\mathcal{O}((MN)^2)$ of when matrix operations are directly applied through $\Psi_p x$. To reduce the complexity, the paper chooses to transform the matrix operation into vector calculations, resulting in

$$\begin{aligned}\mathbf{\Psi}_p\mathbf{x} &= (\mathbf{F}_N \otimes \mathbf{I}_M)\mathbf{\Phi}_p(\mathbf{F}_N^H \otimes \mathbf{I}_M)\mathbf{x} \\ &= (\mathbf{F}_N \otimes \mathbf{I}_M) \\ &\quad \cdot (\Delta^{v_p}\mathbf{\Pi}_{MN}^{l_p}(\mathbf{I}_N \otimes (\mathbf{F}_M^H\mathbf{B}(\tau_i)\mathbf{F}_M))) \cdot (\mathbf{F}_N^H \otimes \mathbf{I}_M)\mathbf{x} \\ &= (\mathbf{F}_N \otimes \mathbf{I}_M) \cdot (\Delta^{v_p}\mathbf{\Pi}_{MN}^{l_p}\mathrm{vec}(\mathbf{F}_M^H\mathbf{B}(\tau_i)\mathbf{F}_M\mathbf{X}_{\mathrm{DD}}\mathbf{F}_N^H)) \\ &= \mathrm{vec}(\mathrm{vec}^{-1}((\Delta^{v_p}\mathbf{\Pi}_{MN}^{l_p}\mathrm{vec}(\mathbf{F}_M^H\mathbf{B}(\tau_i)\mathbf{F}_M\mathbf{X}_{\mathrm{DD}}\mathbf{F}_N^H)) \cdot \mathbf{F}_N).\end{aligned} \tag{33}$$

The computation described above includes the multiplication of two diagonal matrices, i.e., Δ^{v_p} and $\mathbf{B}(\tau_i)$, respectively, a cyclic shift matrix operation $\mathbf{\Pi}_{MN}^{l_p}$, and the FFT and inverse FFT $\mathbf{F}_M\mathbf{X}\mathbf{F}_N^H$ of a 2D matrix $\mathbf{X}$at points $M$and N, respectively. The complexity of the diagonal matrix multiplication is $\mathcal{O}(MN)$, whereas the cyclic shift matrix operation has a complexity of $\mathcal{O}(MN)$. The FFT at point M and the inverse FFT at point N have complexities of $\mathcal{O}(MN\log(M))$ and$\mathcal{O}(MN\log(N))$, respectively.

Therefore, the total complexity of the MF-F algorithm proposed is $\mathcal{O}((MN)\log_2(MN))$. TABLE 4 presents different parameter estimations of the algorithm complexity.

To verify the performance of the algorithm in realistic situations, we constructed a single-input single-output (SISO) OTFS radar sensing system that operated at a carrier frequency of 5.6 GHz using an analog devices, inc. (ADI) Pluto software-defined radio (SDR) and Mathworks Matlab, as shown in Fig. 1 of the OTFS ISAC system. The system was built using two ADI Plutos, with one functioning as an ISAC transceiver and the other as a receiver, as done in [37]. To simulate an actual high-mobility environment, we used the simulated channel on the transmitter side to convey channel information with the ideal DD domain signal, therefore simulating this. The simulation involved examining the relativistic speed, distance, noise power, and simulated

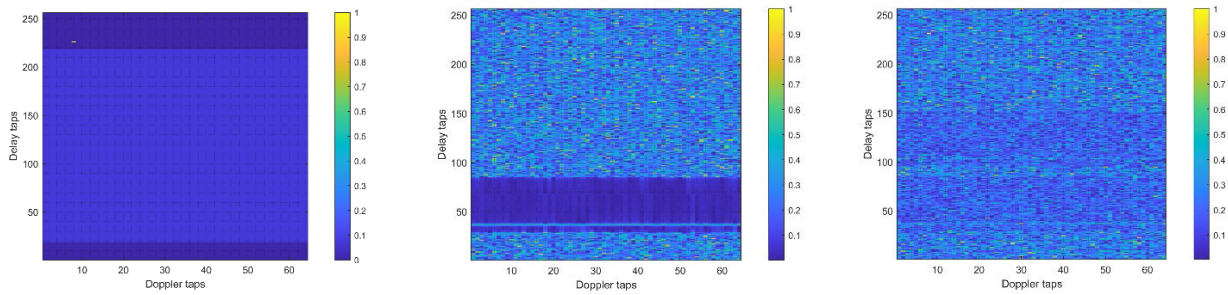

(a) (b) (c)

FIGURE 11. The image before and after the signal passes through the channel. (a) The signal image of the transmitter without passing through the channel; (b) The single-target channel response image; (c) The multi-target channel response image.

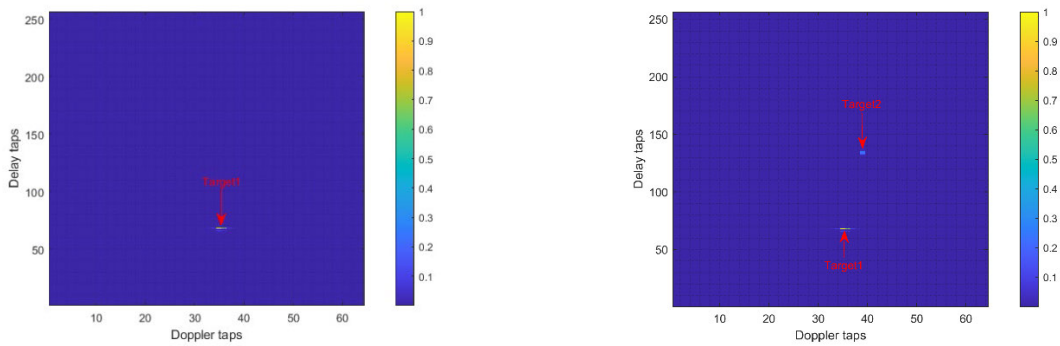

(a) (b)

FIGURE 12. Estimate target results using the MF-F algorithm. (a) The estimated single target; (b) The estimated single target.

TABLE 4. Complexity vs for various algorithms.

Algorithm	Complexity
Proposed MF-F	$\mathcal{O}((MN)\log_2(MN)$
Match filter (MF) [28]	$\mathcal{O}(M^2N^2)$
FFT [19]	$\mathcal{O}((MN)\log_2(MN))$
Fast circular cross-correlation (FCCC) [20]	$\mathcal{O}((MN)\log_2(M)+(MN)\log_2(N))$
Multiple signal classification method (MUSIC) [17]	$\mathcal{O}(M^2N^2+M^3N^3)$

channel parameters of multiple scatterers (i.e., sensing targets), which ultimately revealed the "ground truth" labels channel parameters of multiple scatterers (i.e., sensing targets), which eventually disclosed the "ground truth" labels for evaluating the channel performance. Before conducting super-resolution sensing parameter estimations using the MF-F algorithm, the received signal underwent signal processing, such as frame synchronization, as described in [37]. The detailed simulation parameters are presented in TABLE 5.

We transmitted signals through the CDDS channel. The sensing parameter for single target scene estimation is set $\{(R_1 = 1000\,\text{m}, V_1 = 144\text{km/h})\}$. The parameters for multi-target scene estimation are respectively set as $\{(R_1 = 1000\,\text{m}, V_1 = 144\text{km/h})\}$ and $\{(R_2 = 2000\,\text{m}, V_2 = 360\text{km/h})\}$. The coordinates of the time delay axis and the Doppler frequency shift axis corresponding to the two-parameter sets are $(67.71,\ 35.44)_{M,N}$ and $(133.42,\ 39.12)_{M,N}$. Fig. 11(a)-(c) portrays the images of OTFS transmitter signals before and after encountering single-target and multi-target channel responses. The color of the image of the transmitter signal without passing through the channel is uniform, as depicted in Fig. 11(a). However, upon traversing the CDDS channel, which has time-frequency selective characteristics, the signal incurs damage. As a result, the image presents itself with multiple noisy speckles, as illustrated in Fig. 11(b)-(c). Next, the MF-F algorithm (a type of algorithm) was employed to estimate the target. Fig. 12(a)-(b) presents the image of the first step of the MF. The target coordinates were retrieved from Fig. 12(a) by selecting the axis range's median value at $(68, 35.5)_{M,N}$. Fig. 12(b) displayed estimated target coordinates at $(68, 35.5)_{M,N}$ and $(134, 39)_{M,N}$ respectively. The estimated coordinates from the previous step were then utilized to obtain the second F-step estimation, leading to the acquisition of parameter super-resolution estimation.

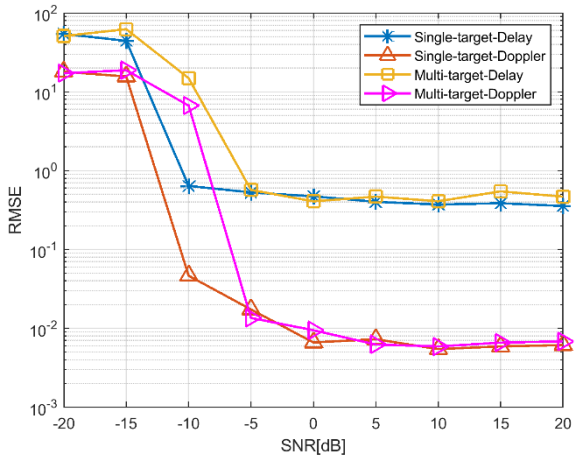

FIGURE 13. RMSE of delay-Doppler sensing parameters.

TABLE 5. Experimental parameters of the SDR platform.

Symbol	Parameter	Value
f_c	Carrier frequency	5.6 GHz
N_c	Number of subcarriers	256
B	Total signal bandwidth	10 MHz
Δf	Subcarriers spacing	39.063 KHz
N_s	Number of symbols (time slots)	64
$\Delta\tau$	Delay resolution	99.9 ns
$\Delta\upsilon$	Doppler resolution	610.3 Hz
SNR	Signal-to-noise ratio	10 dB

As in [37], Monte Carlo experiments were conducted for each scene to compare time delay values and RMSE values of the Doppler shift perception parameter for different scenes. Fig. 13 presents a comparison of sensing parameters for single and multi-target scenes. The results show that, before a low SNR of -5 dB, the time delay values and RMSE values of the Doppler shift sensing parameter for a single target are lower than those of the corresponding parameters for a multi-target. The DD domain channel response pattern is more complex under multi-target conditions, leading to a decrease in estimation accuracy. After -5 dB, the fluctuations of RMSE are minimal, and both the time delay for perception and the RMSE of the Doppler shift remain stable. Based on the results presented, we can conclude that centimeter-level sensing accuracy can be achieved for Doppler sensing parameters. In contrast, the accuracy is limited to decimeters for delay sensing parameters. This limitation is attributed to the simple SDR ISAC system established in this paper, which did not consider hardware limitations in much detail. Further research could focus on addressing these limitations.

V. CONCLUSION

The accuracy of sensing parameter estimation in the ISAC system poses a challenging issue. To address this, the present study investigates the super-resolution ISAC sensing parameter estimation based on the OTFS waveform in a monostatic sensing scenario. This paper introduces a novel algorithm for estimating the perceptual function of the ISAC system. Specifically, the algorithm is for estimating MF-F sensing parameters. To estimate the target parameters, the proposed method employs two steps, which are referred to as MF and F. The MF step is responsible for estimating the integer range of the target parameter on the grid plane; The F step, on the other hand, uses the Fibonacci search method for performing super-resolution estimation within the reduced range acquired from the MF step. In this paper, we develop a sensing system model for the ISAC using a monostatic and determine the input-output relationship of the system's matrices and vectors. Based on these results, the practical scenarios of the SDR hardware platform were used to validate the MF-F algorithm. The effectiveness of the MF-F algorithm was compared to other algorithms (MF, FFT, FCCC, and MUSIC) using numerical simulations. Furthermore, the performance of the algorithm was analyzed based on its multi-target identification accuracies, sensing accuracies, robustness, and complexity. The results indicate that compared to other algorithms, the MF-F algorithm has better perception performance. In addition, the MF-F algorithm exhibits advantageous features such as robustness, low complexity, and superior super-resolution estimation performance. In addition to accurate sensing parameter estimation, future practical applications present challenging research tasks, including resource allocation for ISAC-integrated sensing and communication and interference elimination from ISAC hardware devices in practical scenarios.

APPENDIX A
DERIVATION OF MLE

For brief derivation, consider a single-target scenario. The observed vector $\mathbf{y}$ has a complex Gaussian distribution with mean $h \cdot \mathbf{\Psi}(\tau, \nu)\mathbf{x}$ and variance $\sigma_w^2\mathbf{I}_{NM}$, according to (9)-(11). The maximum likelihood function of $\mathbf{y}$ is provided for a specified set of parameters, yielding

$$f(\mathbf{y}; \boldsymbol{\theta}) = \frac{1}{(\pi\sigma_w^2)^{\frac{NM}{2}}} \exp(-\frac{1}{\sigma_w^2}\|\mathbf{y}-h \cdot \mathbf{\Psi}(\tau, \nu)\mathbf{x}\|^2). \tag{34}$$

Thus, the MLE of $\boldsymbol{\theta}$ that maximizes $f(\mathbf{y}; \boldsymbol{\theta})$is given by

$$\hat{\theta} = (\hat{h}, \hat{\tau}, \hat{\nu}) = \arg\min_{\boldsymbol{\theta}} \|\mathbf{y} - h\mathbf{\Psi}(\tau, \nu)\mathbf{x}\|^2. \tag{35}$$

For the given parameters set $\{(\tau, \nu)\}$, To obtain $\hat{h}$, it is necessary to minimize the following:

$$\begin{aligned} L(h) &= \|\mathbf{y} - h\mathbf{\Psi}(\tau, \nu)\mathbf{x}\|^2 \\ &= (\mathbf{y} - h\mathbf{\Psi}\boldsymbol{x})^H(\mathbf{y} - h\mathbf{\Psi}\boldsymbol{x}) \\ &= \mathbf{y}^H\mathbf{y} - \mathbf{y}^H \cdot h\mathbf{\Psi}\boldsymbol{x} - h(\mathbf{\Psi}\boldsymbol{x})^H \cdot \mathbf{y} + h^2(\mathbf{\Psi}\boldsymbol{x})^H\mathbf{\Psi}\boldsymbol{x}. \end{aligned} \tag{36}$$

By setting the partial derivative of the above (36) w.r.t. h equal to zero, leading

$$\frac{\partial L(h)}{\partial h} = -2 \cdot (\boldsymbol{\Psi x})^H \cdot \mathbf{y} + 2 \cdot h \cdot (\boldsymbol{\Psi x})^H \boldsymbol{\Psi x} \triangleq 0$$
$$\Downarrow$$
$$\hat{h} = \frac{(\boldsymbol{\Psi x})^H \cdot \mathbf{y}}{\|\boldsymbol{\Psi x}\|^2}. \tag{37}$$

Substituting $\hat{h}$in (35) and expanding, we obtain a function of the given variable, which can be written by

$$L(\tau, \nu) = \left\| \mathbf{y} - \hat{h} \cdot \boldsymbol{\Psi}(\tau, \nu) \cdot \mathbf{x} \right\|^2$$
$$= \|\mathbf{y}\|^2 - \frac{\left|(\boldsymbol{\Psi}(\tau, \nu) \cdot \mathbf{x})^H \cdot \mathbf{y}\right|^2}{\|\boldsymbol{\Psi}(\tau, \nu) \cdot \mathbf{x}\|^2}. \tag{38}$$

Thus, the MLE of the parameters set $\{(\tau, \nu)\}$is given as

$$(\hat{\tau}, \hat{\nu}) = \arg\min_{(\tau,\nu)} J(\tau, \nu)$$
$$= \arg\min_{(\tau,\nu)} (\|\mathbf{y}\|^2 - \frac{\left|(\boldsymbol{\Psi}(\tau, \nu) \cdot \mathbf{x})^H \cdot \mathbf{y}\right|^2}{\|\boldsymbol{\Psi}(\tau, \nu) \cdot \mathbf{x}\|^2})$$
$$\Downarrow$$
$$(\hat{\tau}, \hat{\nu}) = \arg\max_{(\tau,\nu)} \frac{\left|(\boldsymbol{\Psi}(\tau, \nu) \cdot \mathbf{x})^H \cdot \mathbf{y}\right|^2}{\|\boldsymbol{\Psi}(\tau, \nu) \cdot \mathbf{x}\|^2}$$
$$\propto \arg\max_{(\tau,\nu)} \left|(\boldsymbol{\Psi}(\tau, \nu) \cdot \mathbf{x})^H \cdot \mathbf{y}\right|^2. \tag{39}$$

The constant coefficient term $\|\boldsymbol{\Psi}(\tau, \nu) \cdot \mathbf{x}\|^2$does not affect ML search results and can be disregarded.

REFERENCES

[1] D. K. P. Tan, "Integrated sensing and communication in 6G: Motivations use cases requirements challenges and future directions," in *Proc. 1st IEEE Int. Online Symp. Joint Commun. Sens. (JCS)*, Feb. 2021, pp. 1–6.

[2] H. Wymeersch, D. Shrestha, C. M. de Lima, V. Yajnanarayana, B. Richerzhagen, M. F. Keskin, K. Schindhelm, A. Ramirez, A. Wolfgang, M. F. de Guzman, K. Haneda, T. Svensson, R. Baldemair, and S. Parkvall, "Integration of communication and sensing in 6G: A joint industrial and academic perspective," in *Proc. IEEE 32nd Annu. Int. Symp. Pers., Indoor Mobile Radio Commun. (PIMRC)*, Sep. 2021, pp. 1–7.

[3] F. Liu, Y. Cui, C. Masouros, J. Xu, T. X. Han, Y. C. Eldar, and S. Buzzi, "Integrated sensing and communications: Toward dual-functional wireless networks for 6G and beyond," *IEEE J. Sel. Areas Commun.*, vol. 40, no. 6, pp. 1728–1767, Jun. 2022.

[4] T. Wild, V. Braun, and H. Viswanathan, "Joint design of communication and sensing for beyond 5G and 6G systems," *IEEE Access*, vol. 9, pp. 30845–30857, 2021.

[5] Q. Qi, X. Chen, A. Khalili, C. Zhong, Z. Zhang, and D. W. K. Ng, "Integrating sensing, computing, and communication in 6G wireless networks: Design and optimization," *IEEE Trans. Commun.*, vol. 70, no. 9, pp. 6212–6227, Sep. 2022.

[6] H. Zhang, H. Zhang, B. Di, M. D. Renzo, Z. Han, H. V. Poor, and L. Song, "Holographic integrated sensing and communication," *IEEE J. Sel. Areas Commun.*, vol. 40, no. 7, pp. 2114–2130, Jul. 2022.

[7] G. Nie, J. Zhang, Y. Zhang, L. Yu, Z. Zhang, Y. Sun, L. Tian, Q. Wang, and L. Xia, "A predictive 6G network with environment sensing enhancement: From radio wave propagation perspective," *China Commun.*, vol. 19, no. 6, pp. 105–122, Jun. 2022.

[8] H. Chen, H. Sarieddeen, T. Ballal, H. Wymeersch, M. Alouini, and T. Y. Al-Naffouri, "A tutorial on terahertz-band localization for 6G communication systems," *IEEE Commun. Surveys Tuts.*, vol. 24, no. 3, pp. 1780–1815, 3rd Quart., 2022.

[9] F. Tang, X. Chen, M. Zhao, and N. Kato, "The roadmap of communication and networking in 6G for the metaverse," *IEEE Wireless Commun.*, early access, Jun. 24, 2022, doi: 10.1109/MWC.019.2100721.

[10] Z. Feng, Z. Wei, X. Chen, H. Yang, Q. Zhang, and P. Zhang, "Joint communication, sensing, and computation enabled 6G intelligent machine system," *IEEE Netw.*, vol. 35, no. 6, pp. 34–42, Nov. 2021.

[11] R. Hadani, "Orthogonal time frequency space modulation," in *Proc. IEEE Wireless Commun. Netw. Conf. (WCNC)*, Mar. 2017, pp. 1–6.

[12] P. Raviteja, Y. Hong, E. Viterbo, and E. Biglieri, "Practical pulse-shaping waveforms for reduced-cyclic-prefix OTFS," *IEEE Trans. Veh. Technol.*, vol. 68, no. 1, pp. 957–961, Jan. 2019.

[13] P. Raviteja, K. T. Phan, and Y. Hong, "Embedded pilot-aided channel estimation for OTFS in delay–Doppler channels," *IEEE Trans. Veh. Technol.*, vol. 68, no. 5, pp. 4906–4917, May 2019.

[14] T. Thaj, E. Viterbo, and Y. Hong, "Orthogonal time sequency multiplexing modulation: Analysis and low-complexity receiver design," *IEEE Trans. Wireless Commun.*, vol. 20, no. 12, pp. 7842–7855, Dec. 2021.

[15] P. Raviteja, K. T. Phan, Y. Hong, and E. Viterbo, "Interference cancellation and iterative detection for orthogonal time frequency space modulation," *IEEE Trans. Wireless Commun.*, vol. 17, no. 10, pp. 6501–6515, Oct. 2018.

[16] Y. Hong, T. Thaj, and E. Viterbo, *Delay-Doppler Communications: Principles and Applications*. San Diego, CA, USA: Academic Press, 2022.

[17] R. Schmidt "Multiple signal classification (MUSIC)," ESL, Cologne, Germany, Tech. Memo TM 1098, 1979.

[18] R. Roy and T. Kailath, "Esprit-estimation of signal parameters via rotational invariance techniques," *IEEE Trans. Acoust., Speech, Signal Process.*, vol. 37, no. 7, pp. 984–995, Jul. 1989.

[19] C. Sturm and W. Wiesbeck, "Waveform design and signal processing aspects for fusion of wireless communications and radar sensing," *Proc. IEEE*, vol. 99, no. 7, pp. 1236–1259, Jul. 2011.

[20] Y. Zeng, Y. Ma, and S. Sun, "Joint radar-communication with cyclic prefixed single carrier waveforms," *IEEE Trans. Veh. Technol.*, vol. 69, no. 4, pp. 4069–4079, Apr. 2020.

[21] K. Wu, J. A. Zhang, X. Huang, and Y. J. Guo, "Integrating low-complexity and flexible sensing into communication systems," *IEEE J. Sel. Areas Commun.*, vol. 40, no. 6, pp. 1873–1889, Jun. 2022.

[22] Z. Gong, S. Liu, L. Li, Y. Huang, and J. Yuan, "Super-resolution delay-Doppler estimation for OTFS radar," in *Proc. IEEE Int. Conf. Commun. (ICC), 5th Workshop Integr. Sens. Commun. (ISAC)*, Rome, Italy, May 2023, pp. 1–4.

[23] Q. Wang, A. Kakkavas, X. Gong, and R. A. Stirling-Gallacher, "Towards integrated sensing and communications for 6G," in *Proc. 2nd IEEE Int. Symp. Joint Commun. Sens. (JCS)*, Seefeld, Austria, Mar. 2022, pp. 1–6, doi: 10.1109/JCS54387.2022.9743516.

[24] M. Temiz, E. Alsusa, and M. W. Baidas, "A dual-function massive MIMO uplink OFDM communication and radar architecture," *IEEE Trans. Cognit. Commun. Netw.*, vol. 8, no. 2, pp. 750–762, Jun. 2022.

[25] L. Gaudio, M. Kobayashi, G. Caire, and G. Colavolpe, "On the effectiveness of OTFS for joint radar parameter estimation and communication," *IEEE Trans. Wireless Commun.*, vol. 19, no. 9, pp. 5951–5965, Sep. 2020.

[26] W. Yuan, Z. Wei, S. Li, J. Yuan, and D. W. K. Ng, "Integrated sensing and communication-assisted orthogonal time frequency space transmission for vehicular networks," *IEEE J. Sel. Topics Signal Process.*, vol. 15, no. 6, pp. 1515–1528, Nov. 2021, doi: 10.1109/JSTSP.2021.3117404.

[27] S. Li, W. Yuan, C. Liu, Z. Wei, J. Yuan, B. Bai, and D. W. K. Ng, "A novel ISAC transmission framework based on spatially-spread orthogonal time frequency space modulation," *IEEE J. Sel. Areas Commun.*, vol. 40, no. 6, pp. 1854–1872, Jun. 2022.

[28] P. Raviteja, K. T. Phan, Y. Hong, and E. Viterbo, "Orthogonal time frequency space (OTFS) modulation based radar system," in *Proc. IEEE Radar Conf. (RadarConf)*, Apr. 2019, pp. 1–6.

[29] L. Gaudio, M. Kobayashi, G. Caire, and G. Colavolpe, "Hybrid digital-analog beamforming and MIMO radar with OTFS modulation," 2020, *arXiv:2009.08785*.

[30] Y. Wu, C. Han, and Z. Chen, "DFT-spread orthogonal time frequency space system with superimposed pilots for terahertz integrated sensing and communication," *IEEE Trans. Wireless Commun.*, early access, Mar. 6, 2023, doi: 10.1109/TWC.2023.3250267.

[31] G. A. Vitetta, D. P. Taylor, and G. Colavolpe, *Wireless Communications: Algorithmic Techniques*. Hoboken, NJ, USA: Wiley, 2013.

[32] D. E. Ferguson, "Fibonaccian searching," *Commun. ACM*, vol. 3, no. 12, p. 648, Dec. 1960.

[33] K. J. Overholt, "Efficiency of the Fibonacci search method," *BIT*, vol. 13, no. 1, pp. 92–96, Mar. 1973.
[34] J. Pan, "Cramer-rao low bound of channel estimation for orthogonal time frequency space modulation system," *IEEE Trans. Veh. Technol.*, vol. 70, no. 10, pp. 9646–9658, Oct. 2021, doi: 10.1109/TVT.2021.3107917.
[35] B. Wang, J. Zhu, X. She, and P. Chen, "Cramer-rao lower bound analysis for OTFS and OFDM modulation systems," 2023, *arXiv:2304.13928*.
[36] S. K. Sengijpta, "Fundamentals of statistical signal processing: Estimation theory," *Technometrics*, vol. 37, no. 4, pp. 465–466, Nov. 1995.
[37] X. Wei, L. Zhang, W. Yuan, F. Liu, S. Li, and Z. Wei, "SDR system design and implementation on delay-Doppler communications and sensing," in *Proc. IEEE Wireless Commun. Netw. Conf. (WCNC)*, Mar. 2023, pp. 1–6, doi: 10.1109/WCNC55385.2023.10118889.

ZHILING TANG received the B.S. and M.S. degrees in communications engineering from the Guilin University of Electronic Technology (GUET), China, in 1997 and 2005, respectively, and the Ph.D. degree in information and communications engineering from Xidian University, China, in 2013. Since 2019, he has been a Professor with the Guilin University of Electronic Technology. His current research interests include signal processing and radio signal recognition technology for wireless communications.

ZHOU JIANG received the B.S. degree in engineering from the Guilin University of Technology, in 2021. He is currently pursuing the M.S. degree with the School of Information and Communication, Guilin University of Electronic Technology. His research interests include radio signal recognition technology for wireless communications and integrated sensing and communication.

WANGHUA PAN was born in Ningdu, Jiangxi, China, in 1979. He received the B.E. degree in aircraft test and launch engineering, the M.S. degree in weapon launch theory and technology, and the Ph.D. degree in flight vehicle design from the National University of Defence Technology (NUDT), China, in 2001, 2004, and 2012, respectively.

Since 2021, he has been a Lecturer with the Guilin University of Electronic Technology (GUET). His research interests include the determination of carrier attitude, satellite navigation, and integrated sensing and communication.

LIZHEN ZENG was born in Hunan, China, in 1979. She received the B.S. degree in electronic information engineering from Xiangtan University, Xiangtan, China, in 2002, and the M.S. degree in communication and information technology from the Guilin University of Electronic Technology, Guilin, China, in 2007.

Since 2008, she has been a Lecturer with the School of Electronic Engineering and Automation, Guilin University of Electronic Technology. She is the author of more than 20 articles and holds three patents. Her current research interests include novel terahertz sensors and its applications and integrated sensing and communication.